Title	Performance assessment of displacement-field estimation of the human left atrium from 4D-CT images using the coherent point drift algorithm
Author(s)	Otani, Tomohiro; Shiga, Mikio; Endo, Shunsuke et al.
Citation	Computers in Biology and Medicine. 2019, 114, p. 103454
Version Type	AM
URL	https://hdl.handle.net/11094/88325
rights	
Note	

Performance assessment of displacement-field estimation of human left atrium from 4D-CT images using the coherent point drift algorithm

Tomohiro Otani[a,*], Mikio Shiga[b], Shunsuke Endo[c], Shigeo Wada[a]

[a]*Department of Mechanical Science and Bioengineering, Graduate School of Engineering Science, Osaka University, 1-3 Machikaneyamacho, Toyonaka, Osaka, 560-8531, Japan*
[b]*Department of Systems Science, School of Engineering Science, Osaka University, 1-3 Machikaneyamacho, Toyonaka, Osaka, 560-8531, Japan*
[c]*Department of Thoracic and Cardiovascular Surgery, Jichi Medical University, 3311-1 Yakushiji, Shimotsuke, Tochigi, 329-0498, Japan*

Abstract

Background: Cardiac four-dimensional computed tomography (4D-CT) imaging is a standard approach used to visualize the left atrium (LA) deformation for clinical diagnosis. However, quantitative evaluation of the LA deformation from 4D-CT images is still a challenging task. We assess the performance of LA displacement-field estimation from 4D-CT images using the coherent point drift (CPD) algorithm, which is a robust point set alignment method based on the expectation–maximization (EM) algorithm.

Methods: Subject-specific LA surfaces at 20 phases/cardiac cycle were reconstructed from 4D-CT images and expressed as sets of triangle elements. The LA surface at the phase which maximizes the LA surface area was assigned as the control LA surface and those at the other 19 phases were assigned as observed LA surfaces. The LA displacement-field was estimated by solving the alignment between the control and observation LA surfaces using CPD.

Results: Global correspondences between the estimated and observed LA surfaces were successfully confirmed by quantitative evaluations using the Dice similarity coefficient (DSC) and areal errors in all phases. Surface distances be-

---

*Corresponding author
Email address: `otani@me.es.osaka-u.ac.jp` (Tomohiro Otani)

tween the estimated and observed LA surfaces ranged within 2 mm, except at the left atrial appendage and boundaries, where incomplete data such as missing or false detections were included in the observed LA surface. We confirmed that the estimated LA surface displacement and its spatial distribution were anisotropic, which is consistent with existing clinical observations.

Conclusion: These results highlight that the LA displacement field estimated by the CPD robustly tracks global LA surface deformation observed in 4D-CT images.

Keywords: Left atrium, Four-dimensional computed tomography (4D-CT), Displacement-field estimation, Coherent point drift (CPD), Point set alignment

---

1. Introduction

The left atrium (LA) is a left-upper heart chamber and transports the oxygenated blood from the pulmonary veins (PVs) to the left ventricle (LV) through the mitral valve (MV). It is widely known that the LA actively functions to modulate LV filling [1] whereas LA pathologic modeling such as LA enlargement, dysfunction and atrial fibrillation are known risk markers that induce thrombus formation in the LA, which is associated with thromboembolic stroke ([2], [3], [4]). Therefore, the assessment of subject-specific LA size and deformation has attracted much interest as a way of understanding LA performance and the risk of ischemic stroke.

Electrocardiogram-gated cardiac computed tomography (CT) is one of the most standard noninvasive methods for visualizing three-dimensional LA shape and its deformation. Cardiac CT scanning over several cardiac cycles using a high temporal resolution multi-detector CT system yields the cardiovascular shape as volumetric image data at various cardiac phase points by synchronizing with the electrocardiogram [5]. This four-dimensional CT (4D-CT) image data allows us to visualize spatiotemporal changes in the LA surface shape. However, because the LA shape is implicitly represented as image data and there are no material points for explicitly tracking the motion, kinematically exact LA wall

deformation cannot be identified directly from 4D-CT images.

Cardiac motion estimation by the medical imaging anlysis based on non-rigid image registration approach has been applied widely for assessment of cardiac function from medical image, such as 4D-CT, magnetic resonance imaging (MRI), and echocardiography, c.f., [6, 7, 8]. In particular, LV function strongly associates with the risk of cardiovascular diseases, and then LV function assessment has been much attracted. Several techniques for assessment of LV function, such as the LV spatio-temporal motion [9] and LV strain [10], were developed based on medical image registration analysis. While, LA function has been paid less attentions, and the LA image registration analyses have been reported in limited cases [11, 12]. LA myocardial wall is relatively thin, which makes imaging analysis of LA motion difficult. Moreover, complexities of the LA shapes and subject-specific differences, especially in the left atrial appendage (LAA) [13], makes even the LA segmentation from medical images difficult. Although several recent existing studies attempted to develop automatic LA segmentation from medical images [14, 15], three-dimensional LA motion estimation by the image registration is challenging so far.

To tackle in this issue, LA motion estimation based on LA surface registration extracted from image data seems to be a better alternative rather than direct image registration. One of the main concepts used to estimate the displacement field from image data is to describe this problem as the alignment problem of two point sets (point set registration), which are extracted from the outline surface of target object in image data at different time phase points, c.f., [16, 17, 18, 19]. The coherent point drift (CPD) algorithm is one effective methods that follows this concept, which was originally proposed in [18]. In the CPD algorithm, two point sets are aligned by solving a probability density estimation problem based on the expectation–maximization (EM) algorithm, i.e., by fitting the Gaussian mixture model (GMM) centroids representing a point set (the control point set) and another point set (the observation point set), with regularizing the displacement-field to maintain motion coherence. This design allows us to apply the alignment of two point sets that are not in one-to-one

3

correspondence, and thus provides robustness to data incompleteness such as noise, outliers, and missing points.

Given these practically useful properties of CPD, a few existing studies have attempted to apply CPD to LA displacement-field estimation [20, 21, 22]. In our previous study, we used CPD to estimate subject-specific LA displacement fields over a cardiac cycle from 4D-CT images and proposed to use this LA displacement field as a moving-wall boundary condition in computational LA blood flow analysis [22]. Computational approaches to blood flow analysis in the LA in individual patients has attracted attention in last half decade for assessing the risk of thrombus formation associated with ischemic stroke [22, 23, 24, 25]. Thus, a technique such as CPD for estimating a subject-specific LA displacement field from 4D-CT images is desirable, not only for evaluating the LA function, but also for analyzing the internal blood flow characteristics while considering subject-specific LA deformation characteristics. However, evaluation of the performance of the LA displacement field estimation by CPD has not been sufficient because of a shortage of clinical datasets and quantitative assessments. Thus, the consistency between the estimated results of the LA displacement field obtained by CPD and original LA surfaces extracted from 4D-CT images is unclear. In addition, CPD involves hyperparameters in its formulation, but their influence on the estimation results has not yet been sufficiently examined.

Here, we assess the performance of CPD-based LA displacement-field estimation taking into account the appropriate setting of hyperparameters. Section 2 introduces an outline of the CPD formulation for general readers and describes the workflow of CPD-based LA displacement-field estimation from 4D-CT images. Section 3 shows the results of CPD parameter adjustment and Section 4 assesses the performance of LA displacement-field estimation over the whole cardiac phase through numerical examples using data from three subjects. Conclusions are presented in Section 5.

4

2. Methods

2.1. Outline of coherent point drift (CPD)

The CPD method proposed in [18] solves the alignment between control point set $\mathbf{X} = \{\mathbf{x}_a \in \mathbb{R}^3 | a = 1...N\}$ and observation point set $\mathbf{Y} = \{\mathbf{y}_b \in \mathbb{R}^3 | b = 1...M\}$ to find the optimal displacement vector of control point set $\mathbf{u} \in \mathbb{R}^{N \times 3}$. For this purpose, CPD assigns the GMM to $\mathbf{X}$ and fits this GMM to $\mathbf{Y}$ using the EM algorithm.

First, a Gaussian distribution with equal isotropic covariances σ^2 is assigned to each control point with displacement, and thus a probability density function with respect to an observation point $p(\mathbf{y}_b | a)$ is given by

$$p(\mathbf{y}_b | a) = \frac{1}{(2\pi\sigma^2)^{\frac{3}{2}}} \exp\left[-\frac{\|\mathbf{y}_b - (\mathbf{x}_a + \mathbf{u}_a)\|^2}{2\sigma^2}\right]. \tag{1}$$

Next, probability density function $p(\mathbf{y}_b)$ of the GMM can be described as the summation form with respect to all control points as

$$p(\mathbf{y}_b) = \sum_{a=1}^{N} P(a)p(\mathbf{y}_b | a), \tag{2}$$

where $P(a)$ is the membership probability and assumed to be a constant ($=1/N$). To account for noise, outliers, and missing points, Equation 2 is modified by adding the uniform distribution $1/M$, given by

$$p(\mathbf{y}_b) = w\frac{1}{M} + (1 - w) \sum_{a=1}^{N} \frac{1}{N} p(\mathbf{y}_b | a), \tag{3}$$

where $w \in [0, 1]$ is a weighting factor. Following Equation 3, the negative log-likelihood function $E(\mathbf{u}, \sigma^2)$ can be finally described as

$$\begin{aligned} E(\mathbf{u}, \sigma^2) &= -\log \prod_{b=1}^{M} p(\mathbf{y}_b) \\ &= -\sum_{b=1}^{M} \log p(\mathbf{y}_b). \end{aligned} \tag{4}$$

The optimal displacement vector $\mathbf{u}$ and covariance σ^2 are obtained by minimizing E using variational calculus. To avoid overfitting due to ill-posed conditions,

this problem is described as a minimization problem considering L2 (Tikhnov) regulation such that

$$\underset{\mathbf{u}\in\mathbb{R}^{N\times3},\sigma^2\in[0,\infty)}{\text{minimize}}\quad f(\mathbf{u},\sigma^2) = E(\mathbf{u},\sigma^2) + \frac{1}{2}\lambda\|\mathbf{u}\|^2, \tag{5}$$

where λ is a regularization parameter. This minimization problem can be solved by the EM algorithm.

The key idea of the CPD algorithm is to model $\mathbf{u}$ as a Gaussian kernel function to produce a coherent motion of the point set, such that

$$\mathbf{u}_p = \sum_{q=1}^{N} G_{pq}\mathbf{w}_q, \tag{6}$$

where $\mathbf{w} \in \mathbb{R}^{N\times3}$ is the base function assigned to each control point and $\mathbf{G} \in \mathbb{R}^{N\times N}$ is a kernel matrix with elements

$$G_{pq} = \exp\left(-\frac{\|\mathbf{x}_p - \mathbf{x}_q\|^2}{2\beta^2}\right), \tag{7}$$

where β is a parameter to determine the span of influence and indices p and q indicate nodes in $\mathbf{X}$.

Gaussian kernel matrix $\mathbf{G}$ is a symmetric and positive-define but dense matrix, and thus appropriate compression of $\mathbf{G}$ may be necessary to save computational memory so that CPD can be used in practice. In the original paper [18], this issue was addressed using low-rank approximation of $\mathbf{G}$ as

$$\begin{aligned}\mathbf{G} &\approx \hat{\mathbf{G}} \\ &= \mathbf{Q}\boldsymbol{\Lambda}\mathbf{Q}^T,\end{aligned} \tag{8}$$

where $\hat{\mathbf{G}}$ is the low-rank approximation of the $\mathbf{G}$, $\boldsymbol{\Lambda} \in \mathbb{R}^{K\times K}$ is a diagonal matrix with the $K(\leq N)$ largest magnitude eigenvalues and matrix $\mathbf{Q} \in \mathbb{R}^{N\times K}$ is a set of the corresponding eigenvectors. Because it is commonly known that the spectrum of eigenvalues of $\mathbf{G}$ decays quickly, c.f., [26], this technique can sufficiently reduce the computational cost ($K \ll N$).

2.2. LA displacement-field estimation from 4D-CT images

Figure 1 summarizes the workflow for estimating the LA displacement field from 4D-CT images using CPD, following our previous study [22]. The present

study uses cardiac 4D-CT images of three subjects without a prior history of cardiac disease (subjects 1,2, and 3). The protocol was approved by the Institutional Review Board of Jichi Medical University.
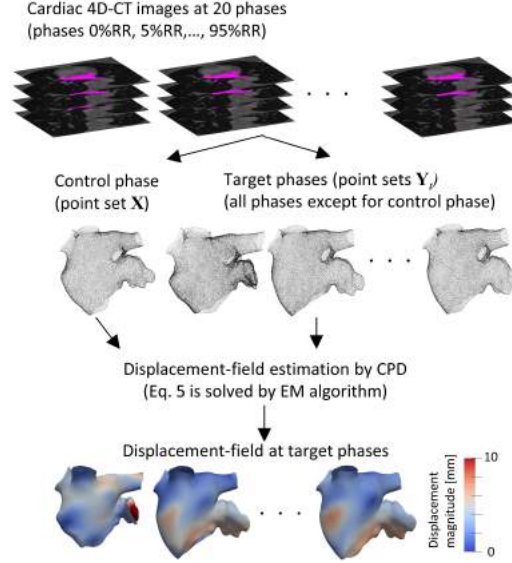

Figure 1: Workflow of coherent point drift (CPD)-based displacement-field estimation of the left atrium (LA) from 4D-CT images. LA surfaces were reconstructed for a total of 20 phases as sets of triangle elements, and element nodes are used as point sets in the CPD-based displacement-field estimation. The LA surface and its nodes at the phase maximizes the LA surface area was assigned as control LA surface and control point set $\mathbf{X}$ and the LA surfaces and these nodes at the other 19 phases were assigned as observed LA surfaces and observation point sets $\mathbf{Y}_t$, t=1,...,19. The LA displacement field was estimated by solving Equation 5 at each phase.

The CT images were acquired during normal sinus rhythm using a 128-slice multi-detector CT scanner (SOMATOM Definition Flash, SIEMENS, Inc., Berlin, Germany). The LA outline surfaces were reconstructed for a total of 20 phases (0% RR, 5% RR...95% RR) during the cardiac cycle, where RR indicates the interval of the R waves, and 0% RR indicates the electrocardiographic ventricular end-diastole. The reconstructed image matrix size was 512×512×240 for subject 1, 512×512×209 for subject 2, and 512×512×310 for subject 3. The

7

in-plane pixel size was 0.39×0.39 mm^2 in subject 1, 0.41×0.41 mm^2 in subject 2, and 0.52×0.52 mm^2 in subject 3. The through-plane slice thicknesses and slice increments were 1.0 mm for all subjects.

The LA shapes were segmented from images at all phases and LA surfaces were reconstructed by a set of linear triangle elements using the Mimics Medical cardiovascular segmentation tool (Version 21.0.0.406; Materialise, Inc., Yokohama, Japan). The distal part of the PVs beyond the first bifurcation and the MV were removed using MeshMixer (Version 3.5.474; Autodesk, Inc., San Rafael, CA). Figure 2 shows the LA shapes of all subjects with maximum LA surface area during cardiac phase (top) and the LA surface area normalized by it at 0% RR (bottom), which shows the extents of LA areal changes ranged from 20-50% in these subjects.

The LA surface and its nodes at the phase when the LA size was largest (65% RR in subject 1, 30% RR in subject 2, and 65% RR in subject 3) were assigned as the control LA surface and control point set $\mathbf{X}$ because the LA surface shape is relatively clear in whole phases. Those at the other 19 phases were used as the observed LA surface and observation point sets $\mathbf{Y}_t$, t=1,...,19.. Numbers of the control point set are 19,883 in subject 1, 21,294 in subject 2, and 21,826 in subject 3. As well, those of observation point sets are 19,215$\pm$1,561 in subject 1, 21259$\pm$1,215 in subject 2, and 20,673$\pm$1,153 in subject 3 (Ave.$\pm$S.D.).

Before CPD, the centers of both $\mathbf{X}$ and $\mathbf{Y}_t$ were set to the origin of the Cartesian coordinate systems and their variations were normalized to one. In the computation, we calculated the K largest eigenvalues with the corresponding eigenvectors to obtain the low-rank approximation of $\mathbf{G}$ in Equation 8 by the implicitly restarted Arnoldi method implemented in the ARPACK-ng library [27]. Note that outliers were almost eliminated in the LA surface reconstruction process, and thus we assumed these effects were negligible and fixed their weight factor to w=0.1. The computation time needed for a displacement-field estimation by CPD was approximately 10 minutes under parallelization with 12 openMP cores using Intel Xeon E5-2650 (2.20 GHz) processors.
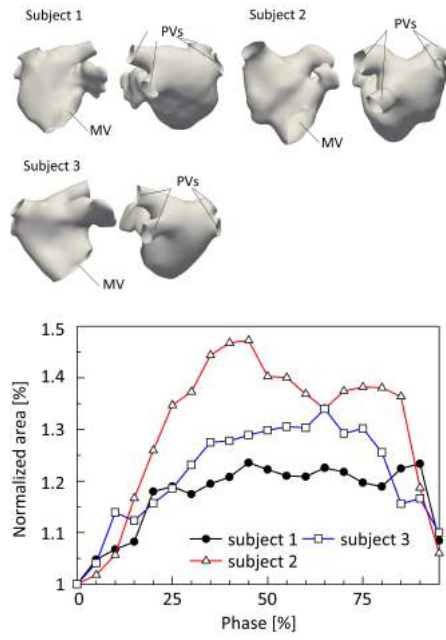
Figure 2: LA shapes with maximum surface area during cardiac phase (top) and time courses of the surface area normalized by the shapes at 0% RR (bottom).

2.3. Evaluations

Effects of hyperparameters β and λ in the CPD formulation and K in the low-rank approximation of $\mathbf{G}$ on the estimation results were examined via a preliminary computation, as described in Section 3. The global correspondence between the estimated and observed LA shapes was evaluated by the Dice similarity coefficient (DSC), areal error, and Hausdorff distance. Volume overlapping between estimated and observed LA shapes are assessed using the DSC which is frequently used for imaging processing. To calculate the DSC from LA surfaces, both estimated and observed LA surfaces are converted to three-dimensional image data. These LA surfaces are projected into Cartesian-grid with the voxel size of 0.25 mm using volume fraction (VOF) ϕ ($0 \le \phi \le 1$) (Fig. 3). The VOF function was calculated by using open-source software V-SDFlib [28]. Assuming that the LA volume consists of the voxel whose VOF is larger than 0.5 and voxels consisting of estimated and observed LA volumes are expressed as the voxel set A and B, respectively. The DSC are defined as

$$\mathrm{DSC}(A, B) = \frac{2|A \cap B|}{|A| + |B|}. \tag{9}$$

The areal error between estimated and observed LA surfaces is calculated by

$$\text{areal error} = \frac{A_{\mathbf{X}}^t}{A_{\mathbf{Y}}^t} - 1, \tag{10}$$

where $A_{\mathbf{X}}^t$ and $A_{\mathbf{Y}}^t$ are the total surface areas of the estimated and observed LA shapes at phase t, respectively.

In Section 4, in addition to the evaluation of global correspondence, the extent of local correspondences between the estimated and observed LA shapes were assessed by the distances between the estimated and observed LA surface in each cardiac phase point. To calculate the minimum distance between a node of the estimated LA surface $\mathbf{x}_c$ and a triangle element of the observed LA surface, a point on triangle element $\mathbf{x}_p$ is represented by the following linear interpolation:

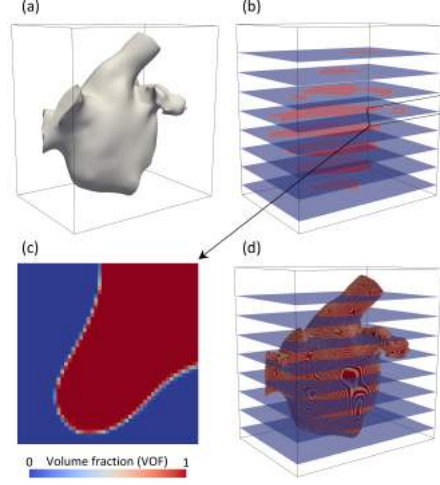$$\mathbf{x}_p = (1 - s_p - t_p)\mathbf{x}_{p0} + s_p\mathbf{x}_{p1} + t_p\mathbf{x}_{p2}, \tag{11}$$

Figure 3: Flowchart to construct LA volume data in three-dimensional image format. The LA surface shape (a) is projected to the Cartesian grid (b) using volume fraction (VOF) function ϕ, shown in (c). LA volume is defined as a set of voxels whose VOF is larger than 0.5 (d).

where $\mathbf{x}_{p0}$, $\mathbf{x}_{p1}$, and $\mathbf{x}_{p2}$ are the element nodes, s_p and t_p are parameters ($s_p, t_p \geq 0, s_p + t_p \leq 1$). The minimum distance between $\mathbf{x}_c$ and $\mathbf{x}_p$ is obtained by minimizing $\|\mathbf{x}_p - \mathbf{x}_c\|$ with respect to s_p and t_p.

Finally, we considered the characteristics of the estimated LA surface deformation by assessing the displacement magnitude and its normal (out-of-plane) and tangential (in-plane) components for the estimated LA surface during a cardiac cycle. The magnitudes of the normal and tangential displacement of node a are respectively defined as $\|\mathbf{u}_a \cdot \mathbf{n}\|$ and $\|\mathbf{u}_a - \mathbf{u}_a \cdot \mathbf{n}\|$, where $\mathbf{n}$ is the unit normal vector of the LA surface.

3. Parameter adjustment

Here, we assess the influences of the hyperparameters and low-rank approximation introduced in Section 2.1 on the CPD-based LA displacement-field estimation results. In this assessment, we calculate the displacement-field estimation from control phase to 0% RR in each subject, which is the phase when the LA size is minimum in a cardiac cycle.

11

3.1. Influences of the degree of low-rank approximation

The influence of K in the low-rank approximation of $\mathbf{G}$ on the estimation results is visualized by plotting the negative log-likelihood E over the iteration process. Figure 4 shows the profiles of E for 100 iteration steps using various $\hat{\mathbf{G}}$ with different $\beta(=0.5, 1, 2$ and $4)$ and K in subject 1, as a representative. When $\beta=2$ for example, E monotonically decays to the same value regardless of K in the initial stage of the iteration process, whereas increases of E occurred during the iteration when K was lower than 50. This occurs at an earlier stage of the iteration process when lower values of K are used. Although these tendencies were found in the other cases using different β, the minimum value of K that maintains a monotonic decay of E depends on β. Because the monotonic decay of E is mathematically guaranteed in the EM algorithm, these results indicate that the use of $\hat{\mathbf{G}}$ with values of K that are too small invalidates the mathematical properties of the EM algorithm, which may output inappropriate solutions. Because the minimum acceptable K depends on β, an appropriate K should be selected for each β in each specific problem. In following sections, we confirm that the E monotonically decays during the iteration process when using $\hat{\mathbf{G}}$ in each subject.

3.2. Influences of the hyperparameters

We assessed the effects of β and λ on the areal error between the estimated and observed LA surfaces using various values for β and λ ($\beta=0.5, 1, 2$, and 4; $\lambda=0.5, 2, 10, 50$, and 100).

In the representative case of subject 1 with $\beta=0.5$ and $\lambda=2$, unrealistic surface intersections of the LA surface were found in the estimation results because of overfitting (Fig. 5(top)). Because β controls the extent of smoothness of the Gaussian kernel (Equation 7) and λ controls the extent of regularization, small values of β and λ may capture local LA deformation but have a higher risk of overfitting. On the contrary, high values of β and λ may overconstrain the LA deformation. Figure 5 (bottom) shows the displacement of the LA surface of the subject 1 for $\beta=2$ and $\lambda=2, 10$, and 100 as an example. Although the spatial
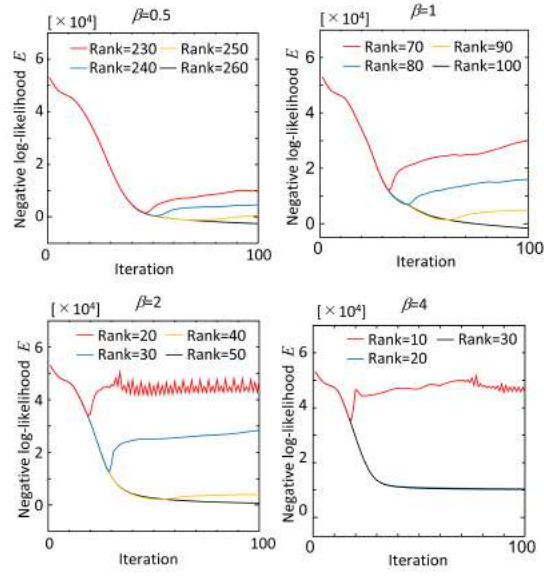
Figure 4: Profiles of negative log-likelihood E during iterations calculated using a low-rank approximation of Gaussian kernel function $\mathbf{G}$ with β=0.5 (top-left), 1 (top-right), 2 (bottom-left), and 4 (bottom-right) and the K largest eigenvalues used for the low-rank approximation of $\mathbf{G}$ in cases of subject 1, as representatives.

13

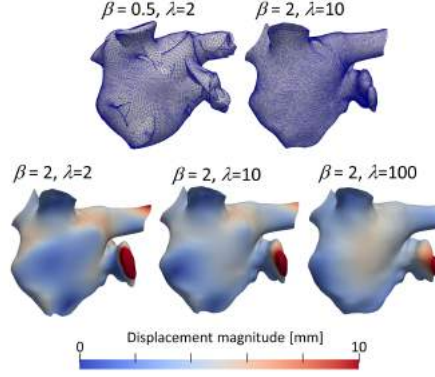distributions of the displacement show similar tendencies, these magnitudes decrease as λ increases.

Figure 5: Representative estimated LA shapes of subject 1 for (β, λ)=(0.5, 2) and (2, 10) (top) and spatial distribution of the areal deformation ratio at 0% RR for (β, λ)=(2, 2), (2, 10), and (2, 100) (bottom).

Influences of the hyperparameters β and λ in the CPD algorithm on the LA displacement-field estimation was assessed by using the DSC. Figure 6 shows values of DSC calculated from estimated results using various values for β and λ in each subject and their average. Note that several cases, in which the VOF function cannot be computed because of surface intersections, are not shown. In all cases in which the VOF can be calculated, DSC was larger than 0.85 and these ranges was less than 0.08. These results indicate that internal volume shapes of the estimated and observed LA surfaces successfully overlap in cases that the DSC can be calculated. In cases of β=0.5 and 1, surface intersections were occurred and the DSC cannot be calculated in almost cases. In cases β = 2, the DSC can be calculated in mot of cases and these values were nearly constant regardless of λ. In cases of β=4, the DSC can be calculated in all cases whereas its values decreased with increasing λ.

As well, influences of the hyperparameters on the areal error are shown in Fig. 7 in each subject and these average. The areal error decreases with increasing λ regardless of β in all subject. For β=0.5 and 1, the areal errors
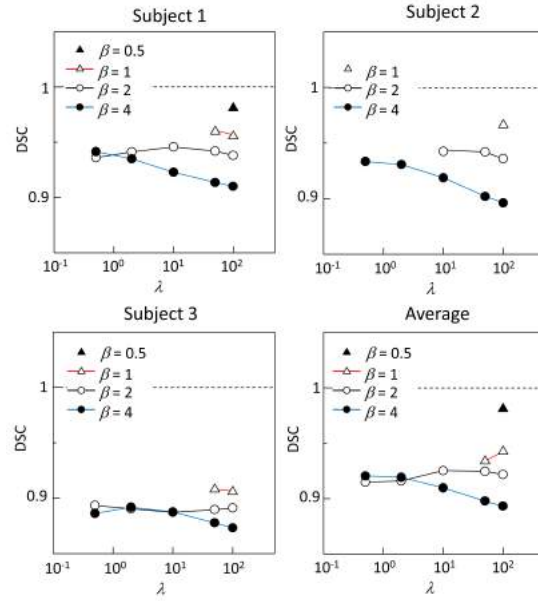
14

Figure 6: Effects of β and λ on the Dice similarity coefficient (DSC) between the estimated and observed LA surfaces in subject 1 (top-left), subject 2 (top-right), subject 3 (bottom-left), and average (bottom-right). Cases in which the VOF function cannot be computed because of surface intersections are not shown.

were relatively high ($¿10\%$) when small λ is set and monotonically decreased as λ increased. For β=2 and 4, decrease degree of areal errors becomes moderate and ranged in $\pm5\%$, while these values becomes negative when β=4 in all subject.
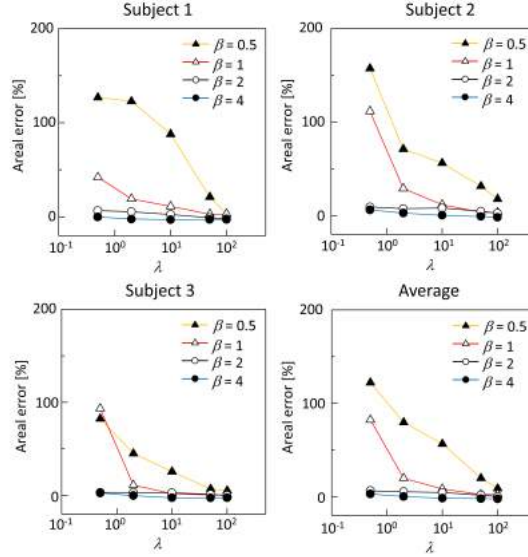

Figure 7: Effects of β and λ on the areal error between the estimated and observed LA surfaces in subject 1 (top-left), subject 2 (top-right), subject 3 (bottom-left), and average (bottom-right).

Following above results, we fixed β=2 in all subject for calculation stability and correspondences in terms of the DSC evaluation. We also selected the value of λ that minimized the magnitude of areal errors from the above parameter set (λ=10 in subject 1 and 100 in subject 2 and 3).

4. Results and discussion

4.1. Displacement-field estimation

This section reports the results for LA displacement-field estimations in three subjects, which were conducted at 20 cardiac phase points. The parameters β, λ, and K were adjusted by the procedures in Section 3.

The global correspondence of the LA surfaces of the estimated and observed LA shapes was confirmed by the DSC and areal error over whole cardiac cycle

16

(Fig. 8). Values of the DSC were higher than 0.92 and the areal ratio were less than ±5% including outliers, in all subjects. These results show that the LA shapes estimated by CPD globally fit well to the observed LA shapes.
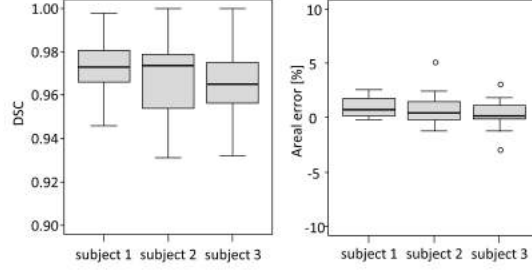

Figure 8: Box plots of Dice similarity coefficient (DSC) and areal error between the estimated and observed LA surfaces at all phase points.

Figure 9 shows representative snapshots of the observed and estimated LA shapes with distances from observation over a cardiac cycle. The whole time courses of these LA shapes over a cardiac cycle are shown in the supplementary movies S1, S2, and S3, for subject 1, 2 and 3, respectively. In all subjects, unrealistic intersections are not found at all phase points. Surface distances are locally high in the boundary domains of the PVs and mitral annulus (MA; junction between the LA and LV) in whole cardiac phase and the LAA, especially at the LA systole phases (e.g., Fig. 9 (bottom-center)). Because boundaries at the PVs and MA cannot be defined explicitly in CT images and CT resolution is still insufficient to capture the LAA structure, especially at the LA systole phase, these regions in the observed LA shapes may be incomplete, i.e., with missing or false detections. In the estimated results, the displacement field of these regions was interpolated based on surrounding point displacements, and then locally and temporally high surface distances may be caused in estimation results.

A quantitative assessment of the surface distances between the observed and estimated LA surfaces was carried out for each subject. Figure 10 shows the distributions of surface distances in each cardiac phase without the outliers
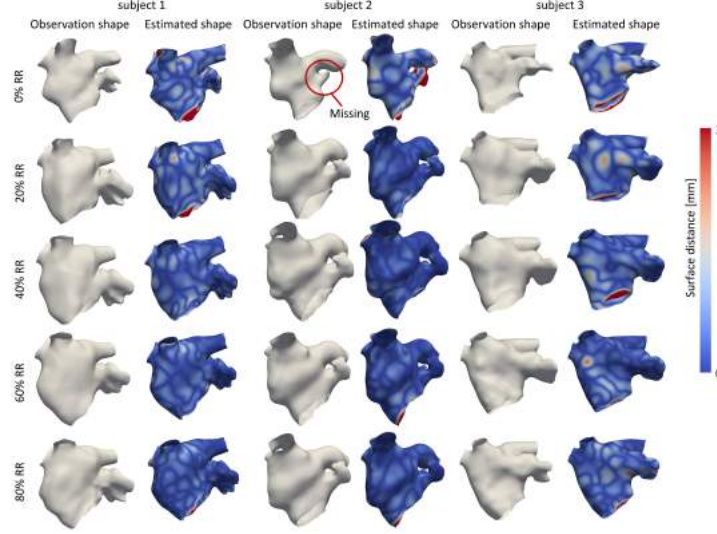
17

Figure 9: Representative snapshots of observed LA shapes and estimated LA shapes with surface distances from the observation in subjects 1 (left), 2 (center), and 3 (right) at phases 0% RR, 20% RR, 40% RR, 60% RR, and 80% RR.

found in the boundary domains and LAA, as shown in Fig. 9. In subject 1, distances mainly range from 0 mm to 1.5 mm and these medians are less than 0.5 mm in all phases. In subjects 2, distances range from 0 mm to 2 mm and medians are less than 0.5 mm in all phases except for phase 95% RR, at which the median is approximately 0.6 mm. These tendencies are also found in subject 3. Because the slice thickness of the CT images of all subjects was 1 mm, we believe that the surface distance observed are acceptable for tracking the LA shape from the 4D-CT images with current spatial resolutions.

Finally, we considered deformation characteristics of the LA surface based on the LA displacement field estimated using CPD. Figure 11 shows spatial distributions of the displacement magnitude of the LA surface and its normal and tangential components at phase 0% RR which is the maximum contraction phase in each subject. The displacement magnitude is highest at the LAA region, whereas the displacement of the superior-posterior side of the LA among the PVs (i.e., the atrial roof) is relatively lower than that of other sides in
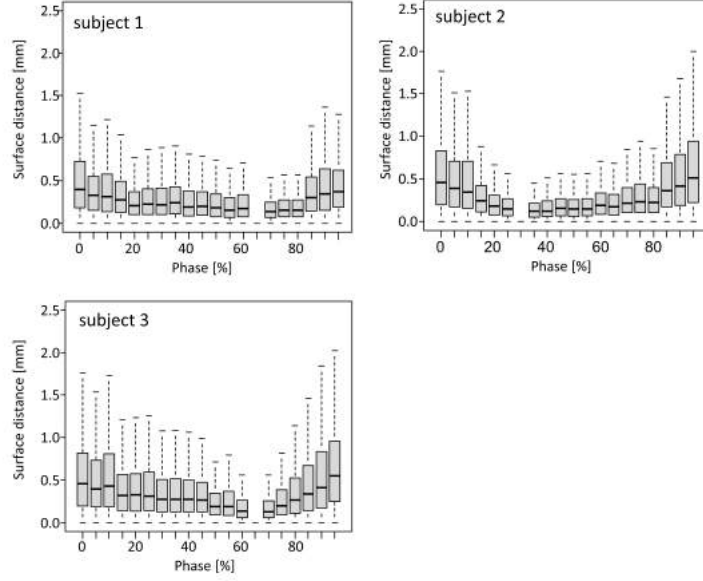
18

Figure 10: Box plots of the distances between the estimated and observed LA shapes at all phase points. Note that outliers are not included in these plots.

all subjects. These relatively lower displacements are also found in *in vivo* measurements in [29] by speckle tracking echocardiography.

The magnitudes of the normal and tangential components of the displacement are comparable, but their spatial distributions show different characteristics (Figure 11 (middle and bottom)). Normal displacement is relatively high on the superior-anterior side of the LA in all subjects, whereas tangential displacement is relatively high on the LAA and inferior side of the LA. It is commonly known that the atrial roof is nearly fixed in the cardiac phase, but the MA cyclically moves along the LV longitudinal axis while maintaining its circular shape in a cardiac cycle [30]. Thus, passive LA deformation associated with the MA motion may cause relatively larger tangential displacement in the inferior side of the LA. These findings suggest that estimated global LA deformation is qualitatively consistent with common clinical knowledge and highlights the necessity of using a spatial displacement-field estimation approach to express subject-specific LA deformation, which includes local anisotropic properties.
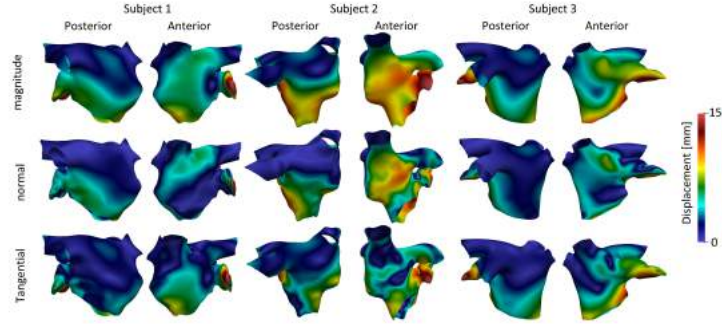
19

Figure 11: Spatial distributions of the displacement magnitude (top) and its normal (middle) and tangential (bottom) components against the left atrial (LA) surface in the estimation results at the maximum contraction phase in each subject: posterior (left) and anterior (right) views.

4.2. Limitations

The displacement-field estimation conducted in this study has four limitations. First, the extent of local LA displacements depends on hyperparameters β and λ, as shown in Fig. 5(bottom), but it is currently difficult to select the most appropriate values. Because the LA shape is not explicitly represented in the CT images, there is so far no methodology that can identify the kinematically exact solution from the displacement-field estimation. Although we believe that the present workflow is robust enough to estimate the global LA displacement field, this limitation should be carefully handled in the quantitative assessment of the LA displacement field, especially in local regions. Second, the effects of CT artifact and segmentation errors on the accuracies of the observation LA shapes were not considered when the CPD parameters were set. We tuned the parameters to fit the estimated LA shape well to the observed LA shape. However, cardiac CT imaging is influenced by motion artifacts [31] and its spatial resolution is still too low to capture complex and dynamic LAA structure, especially in the LA systole, and thus the observed LA surfaces contain errors originating from the CT scanning, segmentation, and reconstruction processes. These influences on the estimated resutls in terms of distances between estimated and observed LA surfaces are shown in Appendix. Because of this limitation, the as-

20

sessment of differences in estimated LA displacement within a few voxels should be also carefully treated. Third, this study used original CPD algorithm [18] while several improved version of the CPD was proposed. There are so many ideas to improve the CPD algorithm because of its outstanding performances and high extensibility, c.f.,[32, 33, 34, 35, 36]. For examples, these modifications achieved automatic parameter optimization for adjusting noise and outliers [33] and the use of landmark points and prescribed structure [32, 36]. Although these updates necessitate additional optimization routine and input information, improved CPD may help us obtain suitable results more easily. Fourth, the workflow employed in this study does not consider temporal interpolation of the LA displacement field, even through 4D-CT imaging outputs sequential volumetric data. In the present workflow, the control point set was fixed and subsequent displacement-field estimation was independently conducted for each phase. Overcoming this drawback may enable us to obtain spatiotemporally reasonable LA motions from the 4D-CT images, which has good potential to not only directly apply the estimation results to the moving wall boundary in the CFD simulation but also improve our physiological knowledge of the LA functions.

5. Conclusions

This study investigated the performance of CPD-based LA displacement-field estimation using cardiac 4D-CT images with the appropriate parameter settings. These results demonstrate that the estimated LA displacement field successfully tracked the observed LA shapes reconstructed from 4D-CT images with interpolated incomplete regions over a cardiac cycle. Furthermore, the estimated LA deformation characteristics with local anisotropy were consistent with existing clinical observations. These results highlight performances and validities of the CPD-based workflow to estimate global LA displacement fields consistent with the LA surface deformation extracted from 4D-CT images.This achievement can reinforce validities of existing studies [20, 22] and help readers

21

conduct the LA deformation estimation and analysis smoothly. Furthermore, assessments of influences of each hyperparameter on LA displacement estimation illustrated these parameter sensitivities and current limitations of the approach conducted. Thus it may be valuable for readers who attempts to adjust hyperparameters for not only the LA surface displacement estimation but also their specific problem.

Finally, a sequential LA displacement field over a cardiac cycle obtained using this framework may be useful not only for subject-specific assessment of the LA function but also for computational LA blood flow analysis that considers clinically consistent LA deformation characteristics. We hope this technique will help improve our understanding of the LA function and its internal blood flow characteristics.

Conflict of interest statement

The authors have no financial or personal interests in the work reported in this paper.

Appendix. **Haudorff distance between estimated and observed LA surfaces**

To consider how far the estimated and observed LA surfaces, we calculated the Hausdorff distances between these point sets. The Hausdorff distance between point sets of estimated and observed LA surfaces $\mathbf{X}$ and $\mathbf{Y}$ are defined as

$$\text{Hausdorff distance}\,(\mathrm{X},\mathrm{Y}) = \max_{\mathbf{x}\in\mathrm{X}}\min_{\mathbf{y}\in\mathrm{Y}} \|\mathbf{x} - \mathbf{y}\|, \tag{12}$$

where $\mathbf{x}$ and $\mathbf{y}$ is the position vectors of the point involved in X and Y, respectively.

Influences of the hyperparameters β and λ in the CPD algorithm on the LA displacement-field estimation was assessed by the Hausdorff distance, as in Section 3. Figure 12 shows the Hausdorff distances calculated from estimated results using various values for β and λ in each subject and their average. Although a few cases show relatively long distances (¿50 mm) at λ=0.5 and β=0.5 and 1 in each subject, these values have certain values ranged from 5 to 10 mm in most cases regardless of the hyperparameters. Since the Hausdorff distance is equivalent to the maximum values of surface distances (Fig. 9), it is thought that the values of Hausdorff distance is determined by the incompleteness of the observed LA surface rather than influences of hyperparameters.

References

[1] B. D. Hoit, Left atrial size and function: Role in prognosis, Journal of the American College of Cardiology 63 (6) (2014) 493–505. `doi:10.1016/j.jacc.2013.10.055`.

[2] P. A. Wolf, R. D. Abbott, W. B. Kannel, Original Contributions Atrial Fibrillation as an Independent Risk Factor for Stroke : The Framingham Study, Stroke 22 (8) (1991) 983–988. `doi:10.1161/01.STR.22.8.983`.

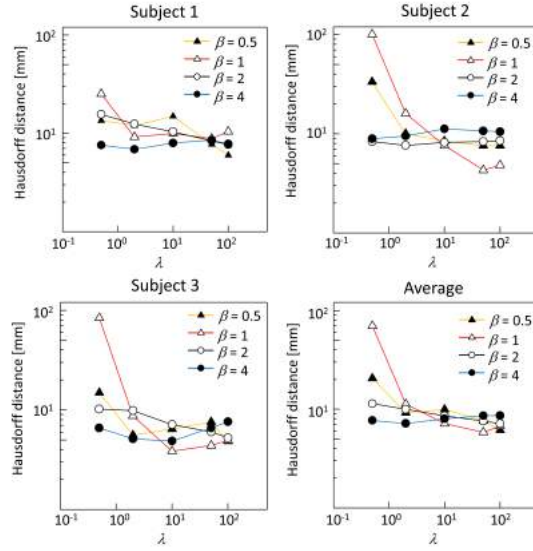[3] E. J. Benjamin, R. B. D'Agostino, A. J. Belanger, P. A. Wolf, D. Levy,

Figure 12: Effects of β and λ on the Hausdorff distance between the estimated and observed LA surfaces in subject 1 (top-left), subject 2 (top-right), subject 3 (bottom-left), and average (bottom-right).

Left Atrial Size and the Risk of Stroke and Death : The Framingham Heart Study, Circulation 92 (4) (1995) 835–841. `doi:10.1161/01.CIR.92.4.835`.

[4] Y. Y. Inoue, A. Alissa, I. M. Khurram, K. Fukumoto, M. Habibi, B. A. Venkatesh, S. L. Zimmerman, S. Nazarian, R. D. Berger, H. Calkins, J. A. Lima, H. Ashikaga, Quantitative Tissue-Tracking Cardiac Magnetic Resonance (CMR) of Left Atrial Deformation and the Risk of Stroke in Patients With Atrial Fibrillation, Journal of the American Heart Association 4 (4) (2015) e001844–e001844. `doi:10.1161/JAHA.115.001844`.

[5] B. Desjardins, E. A. Kazerooni, ECG-Gated Cardiac CT, American Journal of Roentgenology 182 (4) (2004) 993–1010. `doi:10.2214/ajr.182.4.1820993`.

[6] A. Frangi, W. Niessen, M. Viergever, Three-dimensional modeling for functional analysis of cardiac images: a review., IEEE Transactions on Medical Imaging 20 (1) (2001) 2–25. `doi:10.1201/9781420028669.ch9`.

[7] V. Tavakoli, A. A. Amini, A survey of shaped-based registration and segmentation techniques for cardiac images, Computer Vision and Image Understanding 117 (9) (2013) 966–989. `doi:10.1016/j.cviu.2012.11.017`.

[8] A. Sotiras, C. Davatzikos, N. Paragios, Deformable medical image registration: a survey., IEEE transactions on medical imaging 32 (7) (2013) 1153–90. `doi:10.1109/TMI.2013.2265603`.

[9] J. Huang, D. Abendschein, V. G. Dâvila-Român, A. A. Amini, Spatio-temporal tracking of myocardial deformations with a 4-D B-spline model from tagged MRI, IEEE Transactions on Medical Imaging 18 (10) (1999) 957–972. `doi:10.1109/42.811299`.

[10] E. McVeigh, C. Ozturk, Imaging myocardial strain, IEEE Signal Processing Magazine 18 (6) (2001) 44–56. `doi:10.1109/79.962277`.

[11] J. Sra, D. Krum, A. Malloy, M. Vass, B. Belanger, E. Soubelet, R. Vaillant, M. Akhtar, Registration of three-dimensional left atrial computed tomographic images with projection images obtained using fluoroscopy, Circulation 112 (24) (2005) 3763–3768. `doi:10.1161/CIRCULATIONAHA.105.565218`.

[12] J. Sra, S. Ratnakumar, Cardiac image registration of the left atrium and pulmonary veins, Heart Rhythm 5 (4) (2008) 609–617. `doi:10.1016/j.hrthm.2007.11.020`.

[13] R. Beigel, N. C. Wunderlich, S. Y. Ho, R. Arsanjani, R. J. Siegel, The left atrial appendage: Anatomy, function, and noninvasive evaluation, JACC: Cardiovascular Imaging 7 (12) (2014) 1251–1265. `doi:10.1016/j.jcmg.2014.08.009`.

[14] Y. Zheng, D. Yang, M. John, D. Comaniciu, Multi-part modeling and segmentation of left atrium in C-Arm CT for image-guided ablation of atrial fibrillation, IEEE Transactions on Medical Imaging 33 (2) (2014) 318–331. `doi:10.1109/TMI.2013.2284382`.

[15] C. Jin, J. Feng, L. Wang, H. Yu, J. Liu, J. Lu, J. Zhou, Left atrial appendage segmentation and quantitative assisted diagnosis of atrial fibrillation based on fusion of temporal-spatial information, Computers in Biology and Medicine 96 (2018) 52–68. `doi:10.1016/j.compbiomed.2018.03.002`.

[16] H. Chui, A. Rangarajan, A new point matching algorithm for non-rigid registration, Computer Vision and Image Understanding 89 (2-3) (2003) 114–141. `doi:10.1016/S1077-3142(03)00009-2`.

[17] B. Amberg, S. Romdhani, T. Vetter, Optimal step nonrigid ICP algorithms for surface registration, in: IEEE Conference on Computer Vision and Pattern Recognition, IEEE, 2007, pp. 1–8. `doi:10.1300/j001v10n01_01`.

[18] A. Myronenko, X. Song, Point set registration: Coherent point drifts, IEEE Transactions on Pattern Analysis and Machine Intelligence 32 (12) (2010) 2262–2275. `doi:10.1109/TPAMI.2010.46`.

[19] G. K. L. Tam, Z.-Q. Cheng, Y.-K. Lai, F. C. Langbein, Y. Liu, D. Marshall, R. R. Martin, X.-F. Sun, P. L. Rosin, Registration of 3D point clouds and meshes: a survey from rigid to nonrigid., IEEE transactions on visualization and computer graphics 19 (7) (2013) 1199–217. `doi:10.1109/TVCG.2012.310`.

[20] M. Koch, A. Kleinoeder, F. Bourier, J. Hornegger, N. Strobel, Novel method for comparison of pre-planned ablation lines for treatment of atrial fibrillation using a common reference model, Proceedings - International Symposium on Biomedical Imaging (2013) 33–36`doi:10.1109/ISBI.2013.6556405`.

[21] M. Koch, S. Bauer, J. Hornegger, N. Strobel, Towards Deformable Shape Modeling of the Left Atrium Using Non-Rigid Coherent Point Drift Registration, in: Meinzer HP., Deserno T., Handels H., Tolxdorff T. (eds) Bildverarbeitung fr die Medizin 2013. Informatik aktuell., Springer, Berlin, Heidelberg, 2013, pp. 332–337. `doi:10.1007/978-3-642-36480-8_58`.

[22] T. Otani, A. Al-Issa, A. Pourmorteza, E. R. McVeigh, S. Wada, H. Ashik-aga, A Computational Framework for Personalized Blood Flow Analysis in the Human Left Atrium, Annals of Biomedical Engineering (44) (2016) 3284–3294. `doi:10.1007/s10439-016-1590-x`.

[23] R. Koizumi, K. Funamoto, T. Hayase, Y. Kanke, M. Shibata, Y. Shiraishi, T. Yambe, Numerical analysis of hemodynamic changes in the left atrium due to atrial fibrillation, Journal of Biomechanics 48 (3) (2015) 472–478. `doi:10.1016/j.jbiomech.2014.12.025`.

[24] M. Nuñez-Garcia, T. De Potter, E. Silva, O. Camara, G. García-Isla, A. L. Olivares, H. G. Morales, X. Freixa, J. Noailly, C. Butakoff, D. Sanchez-Quintana, Sensitivity analysis of geometrical parameters to study haemo-dynamics and thrombus formation in the left atrial appendage, International Journal for Numerical Methods in Biomedical Engineering 34 (8) (2018) e3100. `doi:10.1002/cnm.3100`.

[25] G. M. Bosi, R. Torii, A. Cook, S. Schievano, L. J. Menezes, R. Rai, G. Burriesci, Computational Fluid Dynamic Analysis of the Left Atrial Appendage to Predict Thrombosis Risk, Frontiers in Cardiovascular Medicine 5 (April) (2018) 1–8. `doi:10.3389/fcvm.2018.00034`.

[26] F. R. Bach, M. I. Jordan, Kernel independent component analysis, Journal of Machine Learning Research 3 (1) (2003) 1–48. `doi:10.1162/153244303768966085`.

[27] ARPACK-ng library, `https://github.com/opencollab/arpack-ng`.

[28] V-SDFlib, `https://vcad-hpsv.riken.jp/en/release_software/VSDFlib/`.

[29] T. F. Cianciulli, M. C. Saccheri, J. A. Lax, A. M. Bermann, D. E. Ferreiro, Two-dimensional speckle tracking echocardiography for the assessment of atrial function, World Journal of Cardiology 2 (7) (2010) 163. `doi:10.4330/wjc.v2.i7.163`.

[30] M. Carlsson, H. Mosén, M. Ugander, T. Buhre, H. Arheden, Atrioventricular plane displacement is the major contributor to left ventricular pumping in healthy adults, athletes, and patients with dilated cardiomyopathy, American Journal of Physiology-Heart and Circulatory Physiology 292 (3) (2006) H1452–H1459. `doi:10.1152/ajpheart.01148.2006`.

[31] P. Rajiah, J. Buethe, S. Halliburton, S. Abbara, S. S. Saboo, K. Kalisz, Artifacts at Cardiac CT: Physics and Solutions, RadioGraphics 36 (7) (2016) 2064–2083. `doi:10.1148/rg.2016160079`.

[32] Y. Hu, E.-J. Rijkhorst, R. Manber, D. Hawkes, D. Barratt, Deformable Vessel-Based Registration Using Landmark-Guided Coherent Point Drift (2010) 60–69`doi:10.1007/978-3-642-15699-1_7`.

[33] P. Wang, P. Wang, Z. G. Qu, Y. H. Gao, Z. K. Shen, A refined coherent point drift (CPD) algorithm for point set registration, Science China Information Sciences 54 (12) (2011) 2639–2646. `doi:10.1007/s11432-011-4465-7`.

[34] Y. Gao, J. Ma, J. Zhao, J. Tian, D. Zhang, A robust and outlier-adaptive method for non-rigid point registration, Pattern Analysis and Applications 17 (2) (2014) 379–388. `doi:10.1007/s10044-013-0324-z`.

[35] S. De Sousa, W. G. Kropatsch, Graph-based point drift: Graph centrality on the registration of point-sets, Pattern Recognition 48 (2) (2015) 368–379. `doi:10.1016/j.patcog.2014.06.011`.

[36] L. Peng, G. Li, M. Xiao, L. Xie, Robust CPD algorithm for non-rigid point set registration based on structure information, PLoS ONE 11 (2) (2016) 1–17. `doi:10.1371/journal.pone.0148483`.